Journal of Geomatics Vol. 16, No. 2, October 2022

Determination of radii of curvature for high resolution geoid models using the harmonic synthesis algorithm

Raaed Mohamed Kamel Hassouna
Department of Civil Engineering, Faculty of Engineering in Shebin El-Kom, Menoufia University,
Shebin El-Kom, Postal code: 32511 Egypt
Email: raaed.hassona@sh-eng.menofia.edu.eg

(Received: Dec 28, 2021; in final form: July 19, 2022)

Abstract: Different types of radii of curvature were assessed for the geoid based on the GECO geopotential model, up to degree and order 2190. The route values of gravity and the three horizontal gravity gradients were computed based on such geopotential model and the angular velocity of the Earth. The investigation was performed on coarse global grids and finer grids covering the Egyptian territory. Respective latitudinal and longitudinal profiles for the geoidal radii were extracted. Comparisons were held with the radii of curvature on the WGS-84 ellipsoid, and with the geoidal radii derived from other models of lower resolutions. Unlike the ellipsoid, the values of the geoidal radii exhibited a rather irregular behaviour that is far from any geographical symmetry. The principal radii of the geoid do not generally occur along the meridian and prime-vertical directions. Such irregularities were found to be more exaggerated with higher degrees. At all investigated resolution levels, the signs of the principal radii assured the convexity of the geoid surface. This enabled to define, compute and compare the Gaussian mean radii for the geoid. The local residual geoidal radii showed a decaying spectral tendency. Also, the results implied that the utilized algorithm proved to be convergent.

Keywords: Geopotential, level surfaces, geoid, differential geometry, radii of curvature, convexity

1. Introduction

According to Gauss, the geoid represents the original mathematical figure of the Earth. In many geodetic applications, the radii of curvature of the geoid have been traditionally assigned a constant value representing the "mean radius of the Earth" (e.g. Bhattacharji 1969). Such spherical approximations have been followed either in a global or regional scale. For example, the determination of geoidal heights as well as the associated topographic reductions necessitate the accurate radius of curvature of the geoid (de Graaff-Hunter 1951; Hirvonen 1954; Müller et al. 1963; Livieratos and Tziavos 1991). This radius significantly differs by about 10 % from that of the ellipsoid (Hirvonen 1954). Also, the geoid is the natural reference system for heights. So, the everywhere convexity of the geoidal surface is an essential property that guarantees its validity as a vertical datum (Vaníček and Santos 2019).

The differential geometry concept was the key for investigating the curvature characteristics of the equipotential surfaces. Over several decades, many works concerning the curvature of level surfaces have been conducted (Burša 1973a, b; Cevallos et al. 2012; Sansò and Sacerdote 2012; Cevallos et al. 2013 and Li 2015).

Almost all of the prescribed investigations have addressed the level surface radii of curvature as a reciprocal measure. Also, some of them have numerically determined the curvatures of the level surfaces. Burša (1973c) has computed the geoidal radii of curvature based on smooth satellite data, up to degree and order 21. However, no study has evaluated updated high degree radii of curvatures of the level surfaces, including the geoid. Furthermore, the convexity of such surfaces has never been computationally judged (Meyer et al. 2004; Vaníček and Santos 2019).

The objectives of the current study are to:

- investigate the geometry of the geoidal surface in terms of its different radii,
- test the convexity of the geoid, and
- investigate the smoothing behaviour of the residual geoidal radii.

The first two tasks are accomplished in both a global and local sense, whereas the third one is performed on a local scheme. The local investigation encounters the Egyptian territory. In all situations, parallel comparisons are held with the radii of the WGS-84 reference ellipsoid. Besides the ultra-high degree GECO (Gilardoni et al. 2016), other geopotential models with different resolutions are used model as a data tool,

Section (2) represents a theoretical overview of the different radii of curvature and shape for level surfaces. In Section (3), the methodology and data, which are used for the current work, are outlined. The results and discussion are presented in Section (4). Finally, in Section (5), the appropriate concluding remarks and recommendations are drawn.

2. Level surface radii of curvature: theoretical concept

Figure 1 depicts the alignment of the right–handed local astronomic system at a given point P on the level surface. In this system, the x–axis points towards the north, the y–axis is taken along the east direction and the z–axis is reckoned towards the zenith.

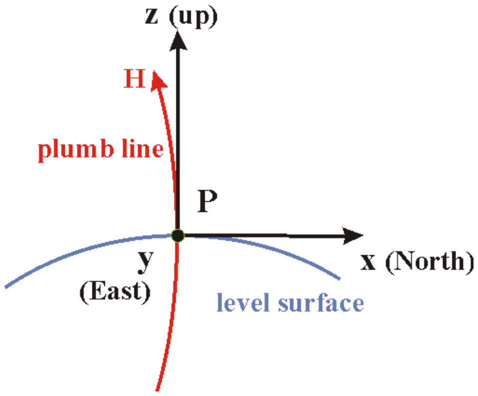

Figure 1. The local astronomic system

The magnitude of gravity at P within this system is given by (Smith 1998; Barthelmes 2013)

$$g=\sqrt{W_x{}^2+W_y{}^2+W_z{}^2}. \tag{1}$$

The corresponding Eötvös tensor is composed of the spatial second derivatives of the potential W, as follows (Torge 2001)

$$\left\|W_{ij}\right\|=\begin{Vmatrix} W_{xx} & W_{xy} & W_{xz} \\ W_{yx} & W_{yy} & W_{yz} \\ W_{zx} & W_{zy} & W_{zz} \end{Vmatrix}. \tag{2}$$

The curvature of any planar normal section, with azimuth α, of the level surface through point P is defined by (Torge 2001)

$$\kappa_\alpha=-\frac{\left(W_{xx}\cos^2\alpha+2W_{xy}\sin\alpha\cos\alpha+W_{yy}\sin^2\alpha\right)}{g}, \tag{3}$$

The minus sign is a convention, such that a resulting positive curvature implies an upward convexity of the normal section of concern (Sharipov 2004; Tu 2017).

Based on Equation (3), the radii of curvature of the level surface in the north and east directions are respectively given by (Torge 2001)

$$R_m=-\frac{g}{W_{xx}}, \tag{4a}$$

$$R_n=-\frac{g}{W_{yy}}. \tag{4b}$$

The principal curvatures of a level surface, $\kappa_{\min}$ and $\kappa_{\max}$, occur at two mutually perpendicular directions. Namely, considering the extrema of Equation (3), such principal azimuths are expressed as follows (Torge 2001)

$$\alpha_{\kappa_{\min}}=\frac{1}{2}\tan^{-1}\left(2\frac{W_{xy}}{W_{xx}-W_{yy}}\right),$$
$$\alpha_{\kappa_{\max}}=\alpha_{\kappa_{\min}}\pm 90^{\circ}. \tag{5}$$

So, based on Equations (5) and (3), the respective maximal and minimal radii of curvature are given by (Torge 2001; Li 2015)

$$R_{\max}=\frac{1}{\kappa_{\min}}=-\frac{g}{W_{xx}+W_{xy}\tan\alpha_{\kappa_{\min}}}, \tag{6a}$$

$$R_{\min}=\frac{1}{\kappa_{\max}}=-\frac{g}{W_{xx}+W_{xy}\tan\alpha_{\kappa_{\max}}}. \tag{6b}$$

Such principal radii are of a pure geometric nature, since they are invariant with respective to any change of the adopted coordinate system (Tu 2017). So, another invariant quantity is the average radius of curvature of the level surface (Sharipov 2004),

$$R_{avg}=\frac{1}{\kappa_{avg}}=\frac{1}{\frac{1}{2}\left(\kappa_{\min}+\kappa_{\max}\right)}=-\frac{2g}{\left(W_{xx}+W_{yy}\right)}, \tag{6c}$$

where κ_{avg} is the average curvature.

Another important invariant feature is the Gaussian (or total) curvature, which is given by (Raussen 2008; Li 2015)

$$\kappa_{Gauss}=\kappa_{\min}\kappa_{\max}=\frac{W_{xx}W_{yy}-W_{xy}{}^2}{g^2}.\left[\frac{1}{\text{length}^2}\right] \tag{7}$$

Specifically, a surface that is elliptic at a given point could be either convex or concave, depending on the common (positive or negative) sign of the principal curvatures (Raussen 2008). In such case, it is possible to define the Gaussian mean radius of curvature as follows

$$R_{mean}=\sqrt{R_{\min}R_{\max}}=\frac{1}{\sqrt{\kappa_{Gauss}}}. \tag{8}$$

So, if existing, R_{mean} would be rather efficient in judging the geometry of level surfaces.

3. Methodology and data

The gravity potential of the Earth, W, is composed of the harmonic gravitational potential and the non-harmonic rotational potential,

$$W=\frac{kM}{r}\sum_{n=0}^{L}\sum_{m=0}^{n}\left(\frac{a}{r}\right)^n\left[(\bar{C}_{nm}\cos m\lambda+\bar{S}_{nm}\sin m\lambda)\bar{P}_{nm}(\cos\theta)\right]$$
$$+\frac{1}{2}\omega^2r^2\sin^2\theta, \tag{9}$$

where
L maximal harmonic degree of the geopotential model,
kM product of the universal gravitational constant by the Earth's mass,
a equatorial radius,
r geocentric radius,
θ geocentric co–latitude,
λ geodetic longitude,
$\overline{C}_{nm}$ fully normalized spherical harmonic C -coefficients of degree n and order m,
$\overline{S}_{nm}$ fully normalized spherical harmonic S -coefficients of degree n and order m,
$\overline{P}_{nm}(\cos\theta)$ fully normalized associated Legendre function of degree n and order m.
ω mean angular velocity of the Earth (7.292115x10^{-5} radian/second).

So, based on Equation (9), the local Cartesian components of gravity can be evaluated as follows (Reed 1973; Tscherning 1976; Tscherning and Poder 1982; Rummel 1997; Barthelmes 2013)

$$W_x = -\frac{kM}{r^2}\left[\sum_{n=0}^{L}\sum_{m=0}^{n}\left(\frac{a}{r}\right)^n (\overline{C}_{nm}\cos m\lambda + \overline{S}_{nm}\sin m\lambda)\frac{d\overline{P}_{nm}(\cos\theta)}{d\theta}\right] - \omega^2 r\sin\theta\cos\theta \tag{10a}$$

$$W_y = -\frac{kM}{r^2\sin\theta}\left[\sum_{n=0}^{L}\sum_{m=0}^{n} m\left(\frac{a}{r}\right)^n \left[(\overline{C}_{nm}\sin m\lambda - \overline{S}_{nm}\cos m\lambda)\overline{P}_{nm}(\cos\theta)\right]\right] + 0 \tag{10b}$$

$$W_z = -\frac{kM}{r^2}\left[\sum_{n=0}^{L}(n+1)\sum_{m=0}^{n}\left(\frac{a}{r}\right)^n \left[(\overline{C}_{nm}\cos m\lambda + \overline{S}_{nm}\sin m\lambda)\overline{P}_{nm}(\cos\theta)\right]\right] + \omega^2 r\sin^2\theta \tag{10c}$$

Also, it can be proved that (Tscherning 1976; Tscherning and Poder 1982; Rummel 1997; Deakin 1998; Zhu 2007; Barthelmes 2013)

$$W_{xx} = -\frac{kM}{r^3}\left[\left[\sum_{n=0}^{N}(n+1)\sum_{m=0}^{n}\left(\frac{a}{r}\right)^n (\overline{C}_{nm}\cos m\lambda + \overline{S}_{nm}\sin m\lambda)\overline{P}_{nm}(\cos\theta)\right] - \left[\sum_{n=0}^{N}\sum_{m=0}^{n}\left(\frac{a}{r}\right)^n (\overline{C}_{nm}\cos m\lambda + \overline{S}_{nm}\sin m\lambda)\frac{d^2\overline{P}_{nm}(\cos\theta)}{d\theta^2}\right]\right] + \omega^2\cos^2\theta \tag{11a}$$

$$W_{xy} = -\frac{kM}{r^3\sin\theta}\left[\left[\cot\theta\sum_{n=0}^{N}\sum_{m=0}^{n}\left(\frac{a}{r}\right)^n m(\overline{C}_{nm}\sin m\lambda - \overline{S}_{nm}\cos m\lambda)\overline{P}_{nm}(\cos\theta)\right] + \left[\sum_{n=0}^{N}\sum_{m=0}^{n}\left(\frac{a}{r}\right)^n m(\overline{C}_{nm}\sin m\lambda - \overline{S}_{nm}\cos m\lambda)\frac{d\overline{P}_{nm}(\cos\theta)}{d\theta}\right]\right] + 0 \tag{11b}$$

$$W_{yy} = -\frac{kM}{r^3}\left[-\left[\cot\theta\sum_{n=0}^{L}\sum_{m=0}^{n}\left(\frac{a}{r}\right)^n (\overline{C}_{nm}\cos m\lambda + \overline{S}_{nm}\sin m\lambda)\frac{d\overline{P}_{nm}(\cos\theta)}{d\theta}\right] + \left[\sum_{n=0}^{L}(n+1)\sum_{m=0}^{n}\left(\frac{a}{r}\right)^n (\overline{C}_{nm}\cos m\lambda + \overline{S}_{nm}\sin m\lambda)\overline{P}_{nm}(\cos\theta)\right] + \left[\frac{1}{\sin^2\theta}\sum_{n=0}^{L}\sum_{m=0}^{n}\left(\frac{a}{r}\right)^n m^2(\overline{C}_{nm}\cos m\lambda + \overline{S}_{nm}\sin m\lambda)\overline{P}_{nm}(\cos\theta)\right]\right] + \omega^2 \tag{11c}$$

A subtle point is that the geoid is one of the level surfaces that extend partially inside the Earth's masses. So, it would be expected to exhibit discontinuities in the second derivatives where density jumps occur (Torge 2001). However, according to Krarup-Runge's theorem, the analytical continuation of the external potential down to the geoid is possible with sufficient practical accuracy (Bjerhammar 1973; Tscherning 1981). Particularly, for points lying on the geoid, the spherical harmonic expansion achieves the harmonic downward continuation of the potential and its derivatives in a natural way simply by amplifying the signal, by using $r_{geoid} < r_{terrain}$ (Barthelmes 2013).

Equations (10), (1) and (11) are used in Section (4) to determine the different radii of curvature for the geoid. This is performed, based on the ultra-high degree GECO model (Gilardoni et al. 2016), the low-degree satellite only model GOCO03S (d/o 250) (Mayer-Gürr et al. 2012) , the ultra-high degree models EIGEN-6C2 (d/o 1949) and SGG-UGM-1 (d/o 2159) (Förste et al. 2012; Liang 2018). For this purpose, the open-source software geopot07 is used. It is capable of synthesizing up to the second order derivatives of the Earth's potential, within the local Cartesian system at any point (Tscherning 1976; Tscherning and Poder 1982; Tscherning et al. 1983; Forsberg and Tscherning 2008; Smith 2010).

4. Results and discussion

4.1 Global investigation of the geoidal geometry

Table 1 lists the statistics of the different types of the geoidal radii of curvature, which were computed over a 5º × 5º global grid, based on GOCO03S model. Table 2 shows the same features, but evaluated from GECO harmonic model. Unlike an ellipsoid of revolution, both tables indicate that the geoidal principal radii do not generally correspond to the meridian and prime-vertical directions. Also, the two tables show that the principal radii possess positive signs, which implies a convexity of the geoid surface at all computational points. Therefore, as shown in the two tables, it was possible to define and compute the Gaussian mean radius of curvature, R_{mean}. It is obvious that the differences among such mean radii and the average ones are generally small.

Table 1. Statistics of the 5º × 5º global geoidal radii of curvature based on GOCO03S (d/o 250) (km)

	Min.	Max.	Mean	Std. Dev.
R_m	6260.117	6480.521	6368.301	25.886
R_n	6299.965	6474.130	6388.995	13.758
$R_{\min}$	6248.500	6431.304	6364.758	23.466
$R_{\max}$	6324.661	6502.624	6392.553	15.244
R_{avg}	6302.701	6448.891	6378.615	18.005
R_{mean}	6302.739	6449.112	6378.635	17.995
$R_{mean} - R_{avg}$	0	0.307	0.020	0.026

Table 2. Statistics of the 5º × 5º global geoidal radii of curvature based on GECO (d/o 2190) (km)

	Min.	Max.	Mean	Std. Dev.
R_m	5655.826	7462.316	6370.516	66.374
R_n	5598.276	7058.731	6389.702	57.622
$R_{\min}$	5573.306	6873.800	6349.438	61.147
$R_{\max}$	5933.936	8234.726	6411.195	71.759
R_{avg}	5747.970	7254.914	6379.890	50.293
R_{mean}	5750.795	7266.092	6380.103	50.718
$R_{mean} - R_{avg}$	0	85.745	0.213	1.819

Obviously, the variation of all radii types in Table 2, as expressed in terms of the standard deviation, are more exaggerated than those in Table 1. This in turn reflects the gain in radii details as computed from the ultra-high degree GECO model.

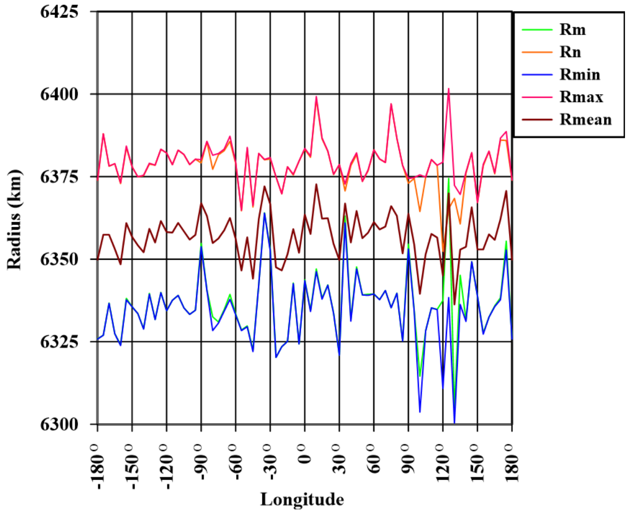

(a): GOCO03S (d/o 250)

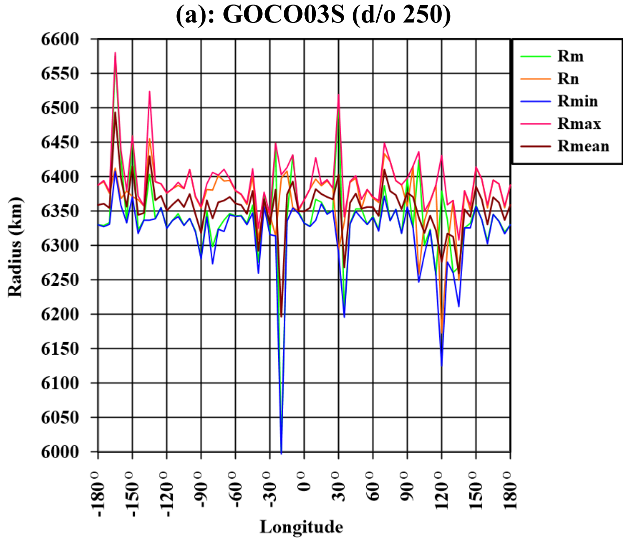

(b): GECO (d/o 2190)

Figure 2. Equatorial profiles for the geoidal radii of curvature

In order to have a deeper global insight, two equatorial profiles were extracted from the global two 5ºx5º sets of meridian, prime-vertical, principal and mean radii of curvatures. Figure (2a) and (2b) depict the details of the two profiles pertaining to GOCO03S and GECO, respectively. Regarding all types of radii of curvature, the rotational symmetry (or the latitude-only dependency) no longer exists. Such rotational anti-symmetry is more pronounced in case of GECO, which exhibits a more oscillatory behaviour.

Tables 3 and 4 show statistical comparisons among the two equatorial profiles depicted in Figure (2a) and (2b), respectively.

Table 3. Statistics of the geoidal radii along the Equator based on GOCO03S (d/o 250) (km)

	Min.	Max.	Mean	Std. Dev.
R_m	6304.242	6374.468	6336.213	11.054
R_n	6352.366	6398.434	6378.160	7.242
$R_{\min}$	6300.393	6363.93	6334.713	10.754
$R_{\max}$	6364.819	6401.689	6379.679	6.416
$R_m - R_{\min}$	0.001	36.091	1.501	5.401
$R_{\max} - R_n$	0	36.399	1.519	5.458
R_{mean}	6336.269	6372.687	6357.154	7.037

Table 4. Statistics of the geoidal radii along the Equator based on GECO (d/o 2190) (km)

	Min.	Max.	Mean	Std. Dev.
R_m	6001.227	6575.318	6340.881	66.462
R_n	6172.599	6454.935	6370.694	41.756
$R_{\min}$	5996.772	6407.722	6318.095	56.509
$R_{\max}$	6307.863	6580.215	6393.674	41.959
$R_m - R_{\min}$	0	254.190	22.786	51.406
$R_{\max} - R_n$	0	258.260	22.980	51.756
R_{mean}	6196.396	6493.396	6355.693	38.572

Likewise, two profiles were extracted from the two global grids of radii of curvatures, but along Greenwich meridian. Figure (3a) and (3b) illustrate these profiles. Both profiles are anti-symmetric with respect to the equatorial plane, a fact which is more exaggerated in Figure (3b) that corresponds to GECO model. Tables 5 and 6 list the corresponding statistics.

Figure (4a) and (4b) depict the variation of the GECO geoidal radii of curvature with longitude at the poles. The two poles possess different mean and principal radii. Also, it was noticed that the patterns in Figure (4) mirror those pertaining to the western hemisphere, which acted as a validation tool for the computational algorithm.

Table 5. Statistics of the geoidal radii along Greenwich meridian based on GOCO03S (d/o 250) (km)

	Min.	Max.	Mean	Std. Dev.
R_m	6335.483	6403.669	6368.977	22.814
R_n	6371.961	6411.633	6390.273	10.192
$R_{\min}$	6335.410	6400.789	6367.279	21.004
$R_{\max}$	6372.112	6416.979	6391.976	11.680
$R_m - R_{\min}$	0	9.324	1.698	3.001
$R_{\max} - R_n$	0	9.330	1.703	3.006
R_{mean}	6356.213	6406.098	6379.613	15.951

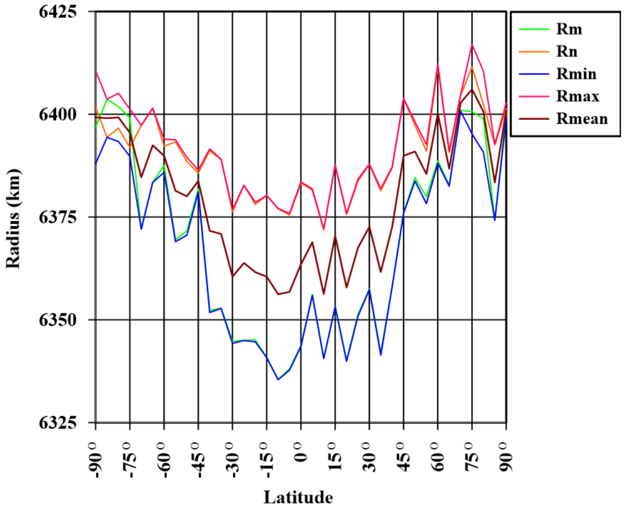

(a): GOCO03S (d/o 250)

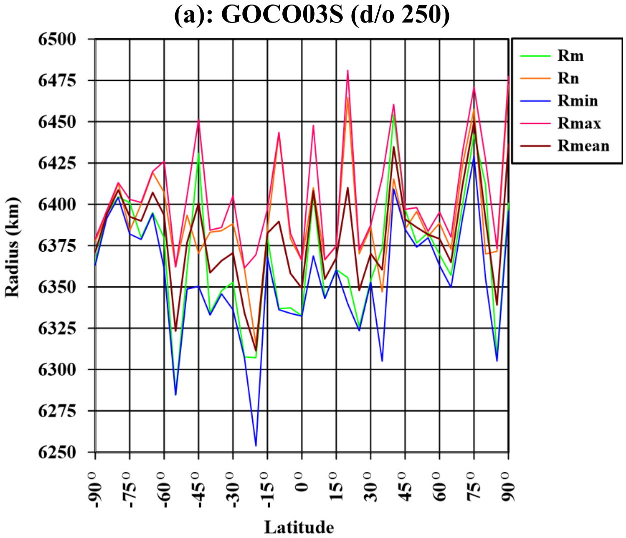

(b): GECO (d/o 2190)

Figure 3. Greenwich profiles for the geoidal radii

Table 6. Statistics of the geoidal radii along Greenwich meridian based on GECO (d/o 2190) (km)

	Min.	Max.	Mean	Std. Dev.
R_m	6284.696	6454.208	6368.891	38.628
R_n	6315.068	6472.430	6391.256	31.846
$R_{\min}$	6253.770	6429.035	6355.037	35.991
$R_{\max}$	6361.470	6481.104	6405.257	33.591
$R_m - R_{\min}$	0.043	80.486	13.854	20.823
$R_{\max} - R_n$	0.044	80.994	14.000	21.021
R_{mean}	6311.386	6449.996	6380.076	30.393

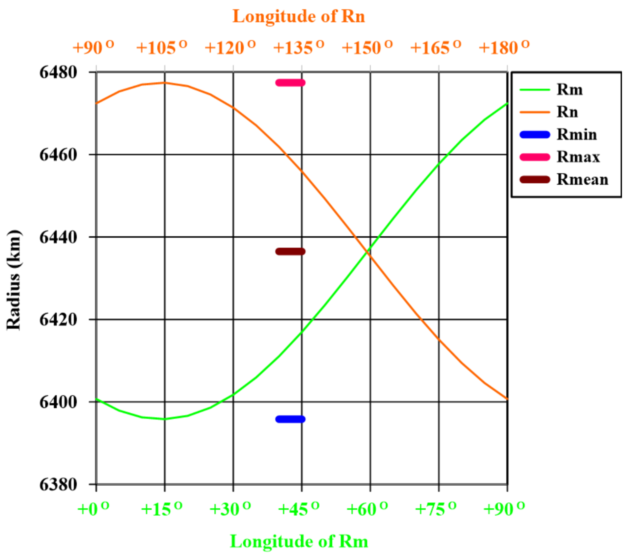

(a): North pole

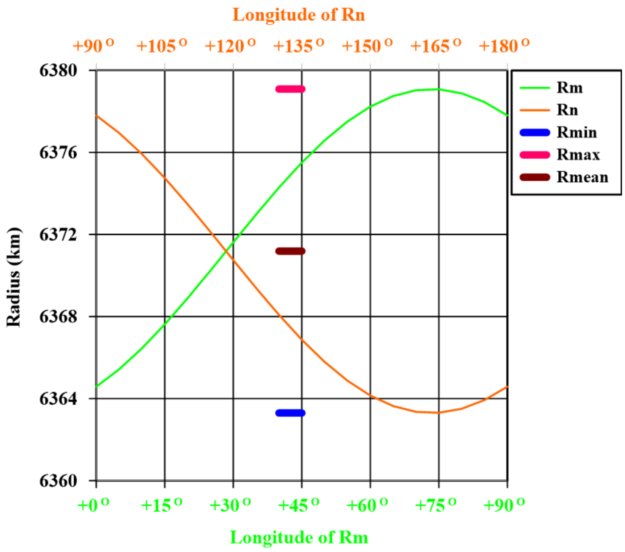

(b): South pole

Figure 4. The geoidal radii of curvatures at the poles based on GECO (d/o 2190)

For the sake of comparison, 5º × 5º global grids for the meridian, prime-vertical and mean radii of curvature were evaluated for the WGS-84 reference ellipsoid (Jekeli, 2006). Tables 7 and 8 list the statistical comparison between the GECO and GOCO03S geoidal radii and those of WGS-84. While the small mean values in the two tables imply a good overall behaviour of the WGS-84 geocentric ellipsoid in approximating the geoid, the associated large ranges and standard deviations could reflect the regional irregularities of the geoidal radii.

Figure 5a shows a global contour map for the differences among the geoidal mean radii from GOCO03S model and those of WGS-84. This map shows significant regional differences, which are neither rotationally nor equatorially symmetric. Such result is more pronounced in Figure (5b), which illustrates another comparative contour map, but regarding GECO model.

Table 7. Statistical comparison among the 5ºx5º global GOCO03S geoidal radii and those of WGS-84 (km)

	Min.	Max.	Mean	Std. Dev.
$R_m - R_{m_{WGS\text{-}84}}$	−104.442	102.153	−0.017	12.861
$R_n - R_{n_{WGS\text{-}84}}$	−81.988	89.374	−0.147	11.466
$R_{mean} - R_{mean_{WGS\text{-}84}}$	−70.796	60.283	−0.082	9.869

Table 8. Statistical comparison among the 5ºx5º global GECO geoidal radii and those of WGS-84 (km)

	Min.	Max.	Mean	Std. Dev.
$R_m - R_{m_{WGS\text{-}84}}$	−711.556	1110.939	2.199	62.679
$R_n - R_{n_{WGS\text{-}84}}$	−786.896	675.250	0.559	57.087
$R_{mean} - R_{mean_{WGS\text{-}84}}$	−619.988	898.683	1.386	48.496

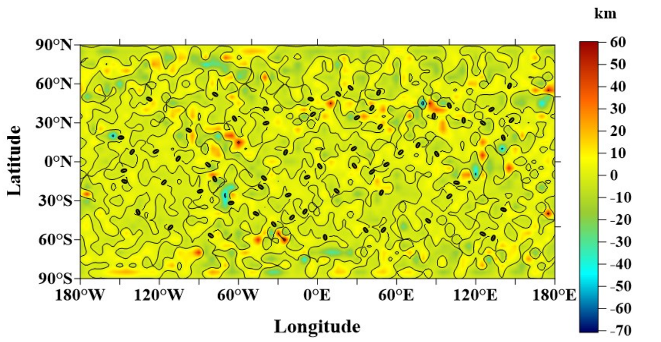

(a): (GOCO03S minus WGS-84)

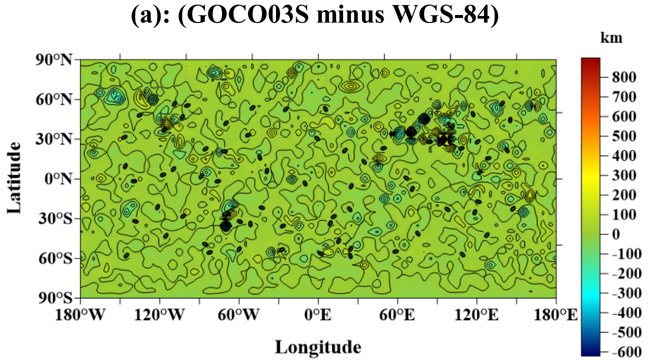

(b): (GECO minus WGS-84)

Figure 5. Global contour maps for the differences among the geoidal and WGS-84 mean radii of curvature (Interval: 50 km)

4.2 Local application to the Egyptian territory

Firstly, local 10′ × 10′ grids of the geoidal radii of curvature were computed over the Egyptian territory, based on GECO model. These grids cover the window $(22°\ N\ \leq \varphi \leq\ 32°\ N;\ 25°\ E\ \leq \lambda \leq\ 36°\ E)$.

Table 9 shows the corresponding statistics. Again, the principal radii are all positive. This result ascertains the convexity of the geoidal surface at such local scale with a much finer resolution. The large departures of the principal radii from those in the north and east directions are obvious in Table 9. Each pair of these radii types generally occur at different azimuths. This is easy to infer from Table (10), which lists the statistics of the azimuths of the geoidal maximal radii based on GECO. Obviously, these azimuths exhibit a broad range of values around the east direction.

Table 9. Statistics of the 10′x10′ grids of the geoidal radii for Egypt based on GECO (d/o 2190) (km)

	Min.	Max.	Mean	Std. Dev.
R_m	6027.371	6614.634	6347.017	39.104
R_n	5863.951	6991.018	6383.203	57.087
$R_{\min}$	5835.614	6473.656	6332.606	45.206
$R_{\max}$	6136.712	7007.131	6397.845	52.579
R_{avg}	5982.377	6656.605	6364.919	38.596
R_{mean}	5984.270	6664.949	6365.073	38.706
$R_{mean} - R_{avg}$	0	11.924	0.153	0.503

Table 10. Statistics of the 10′x10′ values of the azimuths of the geoidal maximal radii for Egypt based on GECO (d/o 2190) (arc-degree)

	Min.	Max.	Mean	Std. Dev.
$\alpha_{\max}$	0	179.8	90.1	30.9

Figure (6a) and (6b) show the local profiles of the geoidal radii along the 27ºN latitude and the 30ºE meridian, respectively. These two figures agree with the general observations obtained from the global profiles in Figure (2) and (3), respectively.

Furthermore, it was decided to perform a degree-wise investigation of the residual geoidal radii of curvature. For this purpose, other 10′x10′ local grids were established over Egypt, based on WGS-84 ellipsoid; and the GOCO03S (d/o 250), EIGEN-6C2 (d/o 1949) and SGG-UGM-1 (d/o 2159) geopotential models. In order to perform the investigation at appropriate spectral-degree intervals, EIGEN-6C2 model was utilized at two stages: firstly up to d/o 1000 and then up to d/o 1800.

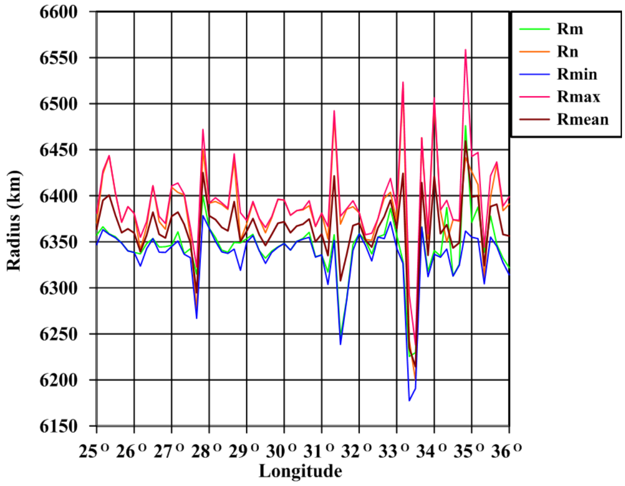

(a): Profiles along the 27ºN latitude

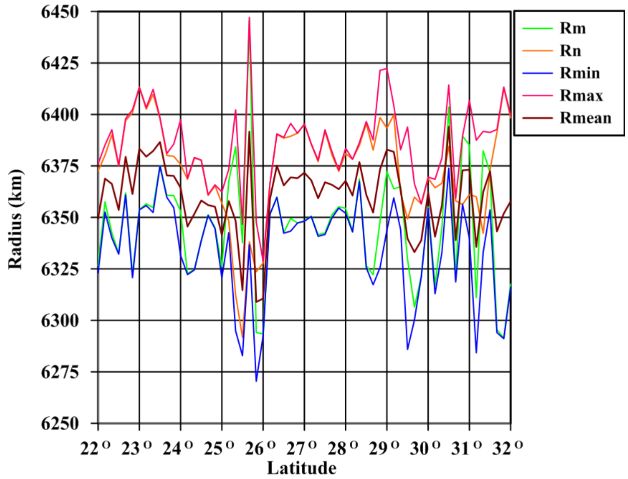

(b): Profiles along the 30ºE meridian

Figure 6. Local profiles for the geoidal radii of curvature from GECO

Table 11–15 list statistical comparisons for the 10′x10′ residual grids of the different geoidal radii types. Such residual values are the result of subtracting the different radii types pertaining to WGS-84, GOCO03S, EIGEN-6C2 (up to d/o 1000), EIGEN-6C2 (up to d/o 1800) and SGG-UGM-1; from those corresponding to GECO model. On one hand, the five tables show that the removal of the contributions of WGS-84 ellipsoid produced remarkably small mean, minimal and maximal residuals, while the corresponding standard deviations are nearly the same as those of GECO model. Again, this reflects the large local irregularity of the geoidal radii with respect to those of a reference ellipsoid. On the other hand, the removal of the radii derived from the remaining three harmonic models lead to an elegantly progressive smoothness of the residuals. Namely, such smoothness increases dramatically with the removal of higher harmonic degrees.

Table 11. Statistics of the 10′x10′ grids of the residual R_m values (km)

Residual R_m	Min.	Max.	Mean	Std. Dev.
N/ A (GECO)	6027.371	6614.634	6347.017	39.104
GECO–WGS-84	–323.367	264.055	–1.656	39.161
GECO–GOCO03S	–313.898	273.407	–0.341	37.990
GECO–d/o 1000	–230.617	202.915	–0.338	28.395
GECO–d/o 1800	–138.883	95.816	–0.379	17.136
GECO–d/o 2159	–24.805	22.797	0.472	5.826

Table 12. Statistics of the 10′ × 10′ grids of the residual R_n values (km)

Residual R_n	Min.	Max.	Mean	Std. Dev.
N/ A (GECO)	5863.951	6991.018	6383.203	57.087
GECO–WGS-84	–519.105	607.645	0.628	57.066
GECO–GOCO03S	–523.772	590.560	0.603	55.936
GECO–d/o 1000	–322.971	441.996	0.201	33.707
GECO–d/o 1800	–123.692	138.350	0.141	18.500
GECO–d/o 2159	–35.872	31.748	0.007	6.387

Table 13. Statistics of the 10′ × 10′ grids of the residual $R_{\min}$ values (km)

Residual $R_{\min}$	Min.	Max.	Mean	Std. Dev.
N/ A (GECO)	5835.614	6473.656	6332.606	45.206
GECO–WGS-84	–514.494	120.477	–16.067	45.521
GECO–GOCO03S	–501.491	128.597	–13.786	44.645
GECO–d/o 1000	–300.581	166.759	–4.601	30.241
GECO–d/o 1800	–128.121	134.858	–1.404	17.231
GECO–d/o 2159	–29.964	29.157	0.529	6.085

Table 14. Statistics of the 10′x10′ grids of the residual $R_{\max}$ values (km)

Residual $R_{\max}$	Min.	Max.	Mean	Std. Dev.
N/ A (GECO)	6136.712	7007.131	6397.845	52.579
GECO–WGS-84	–246.344	623.864	15.270	52.477
GECO–GOCO03S	–252.042	601.229	14.270	51.445
GECO–d/o 1000	–272.273	417.436	4.578	32.522
GECO–d/o 1800	–133.447	135.748	1.201	18.135
GECO–d/o 2159	–32.387	33.129	–0.052	6.276

Table 15. Statistics of the 10′ × 10′ grids of the residual R_{mean} values (km)

Residual R_{mean}	Min.	Max.	Mean	Std. Dev.
N/ A (GECO)	5984.270	6664.949	6365.073	38.706
GECO–WGS-84	–382.29	297.968	–0.529	38.694
GECO–GOCO03S	–378.607	288.741	0.118	37.793
GECO–d/o 1000	–219.898	230.075	–0.067	25.240
GECO–d/o 1800	–112.969	95.071	–0.119	14.430
GECO–d/o 2159	–22.250	24.219	0.240	5.023

It should be noted that none of the geoidal radii is harmonic, since not only the harmonic gravitational part, but also the rotational potential contributes to their values. Although this rotational contribution is not a direct additive counterpart of the geoidal radii, it could have been someway minimized if not cancelled at all from the residuals in Table 11–15. This speculation could hold true, keeping in mind the larger standard deviations of the residuals relevant to WGS-84 in those five tables and in Table 8. Such large standard deviations could be due to the pure geometrical nature of the ellipsoidal radii.

It is worthy to view the decay of the geoidal radii residuals in Table 11–15 from another perspective. Namely, this attenuation could assure the convergence of the algorithm followed in the current work, in which the geoidal radii are derived based on harmonic models.

Finally, two local profiles for the geoidal mean radii were extracted along the 27ºN parallel of latitude and the 30ºE meridian. These two profiles are plotted in Figure (7a) and (7b), respectively. Obviously, the mean radii profiles corresponding to GOCO0S possess low resolution smooth trends. Alternatively, those pertaining to the higher resolutions from d/o 1000 to 2159 show irregular rough behaviours. In particular, the coherency of such rough profiles with those of the GECO model agrees with the dramatic decay of their residuals in Table 11–15. Therefore, such coherency again ascertains the convergence of the current algorithm.

5. Concluding remarks and recommendations

The computation of the geoidal radii based on ultra-high degree geopotential harmonic models proved to be an efficient and convergent algorithm. Both the global and local investigations indicated that the geoidal radii of curvature exhibit strongly rapid variations. These radii possess neither a longitudinal symmetry nor a latitudinal dependency. Unlike the ellipsoid, the geoidal principal radii do not generally occur along the north and east directions.

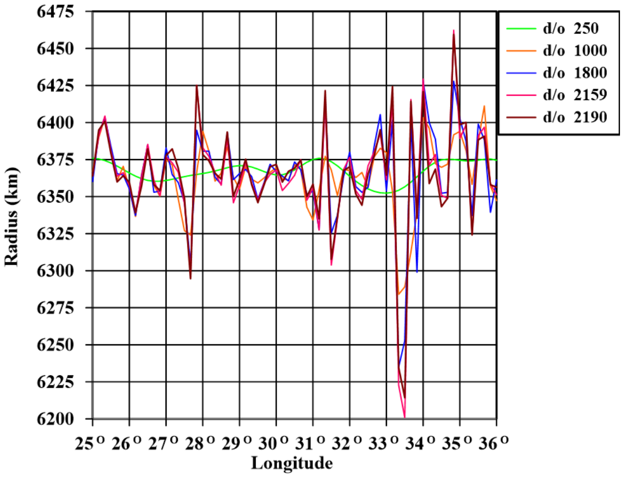

(a): Profiles along the 27ºN latitude

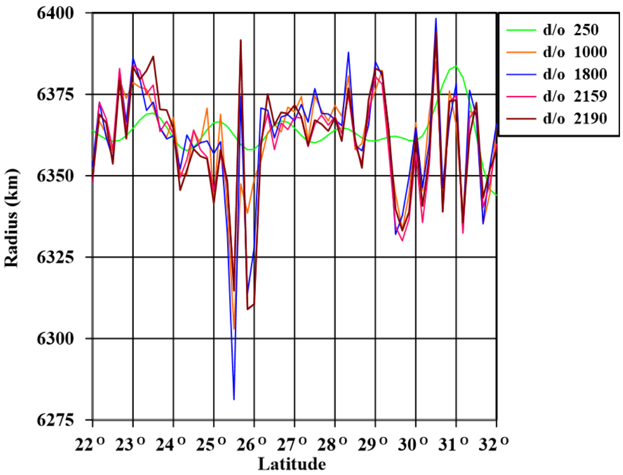

(b): Profiles along the 30ºE meridian

Figure 7. Local profiles for the geoidal mean radii based on different harmonic degrees

In general, at any point, there could be remarkable differences among the meridian and prime-vertical radii and the corresponding principal values.

The geoid is a smooth surface that is convex everywhere at seas and on land (Meyer et al. 2004; Vaníček and Santos 2019). Such pioneered opinions were verified in the current work, provided the positive principal radii of the geoid at all encountered evaluation points. Based on this property, it was possible to define and assess the Gaussian radius of curvature for the geoid.

It is recommended to further apply the algorithm presented in the current wok to assess the geoidal radii of curvature over any desired geographical window. Obviously, the target resolution of the application in question would judge the maximal degree of the geopotential model of choice. Particularly, some simple surveying tasks might necessitate a realistic value for the geoidal radius along any direction, for example, the reduction of long slope distances to mean sea level.

Also, it is well known that the torsion balance devices are an efficient tool for determining the terrestrial components of the curvature tensor (e.g. Völgyesi 2015). So, co-locating torsion balance devices with gravimeters, mixed gravity and gravity gradient observations can be collected. After the reduction of these data down to the geoid, detailed (or full-resolution) local geoidal radii of curvature can be assessed, based on the first principles given in Section (2). Furthermore, in view of the smooth behaviour of the residual geoidal radii, the remove-restore strategy might be tried to compute robust local geoidal radii at points with no data. Namely, ultra-high degree model-based radii may be removed from those evaluated from scattered dense co-located and gravity and torsion balance data. Then, the resulting residual radii of the geoid are interpolated into the target new points, and added back to the respective values that are derived from the same harmonic model. This stands in analogy with the remove-restore technique for local gravity field modelling.

The Gaussian radius of the geoid may be used for defining the solid spherical harmonics during the solutions for global harmonic models. This proposal stems from the validity of the Gaussian curvature for such task. This harmonic analysis strategy may be tried and compared with the spherical and ellipsoidal harmonic analysis schemes. These comparisons might be extended to check the efficiency of the corresponding subsequent harmonic synthesis results, regarding their fit to the observed gravitational data. Accordingly, a further future application may be to investigate the use of accurate mean geoidal radii in local geoid determination; and the associated topographic reductions.

Finally, the current algorithm may be generalized to evaluate the different types of radii of curvature for level surfaces through surface terrain points. In this circumstance, a digital terrain model, or the elevations of the scattered points of concern, would be an additional requirement. When applicable, this future outlook could be extended to the above outlined recommendations. In such cases, no doubt would exist regarding the convergence of the harmonic series.

Acknowledgments

Dr. D.A. Smith is acknowledged for releasing program Geopot07 as public domain. Also, three anonymous reviewers are thanked for their effort.

References

Barthelmes F. (2013). Definition of Functionals of the Geopotential and Their Calculation from Spherical Harmonic Models: Theory and formulas used by the calculation service of the International Centre for Global Earth Models (ICGEM). GFZ Scientific Technical Report STR09/0. DOI: 10.2312/GFZ.b103-0902-26.

Bhattacharji J.C. (1969). Modified Earth Model Free-air Gravity Anomaly for Use in Vening Meinesz's Formula, Studia geoph. et geod.,13(1969), pp. 373–389.

Bjerhammar A. (1973). On the Discrete Boundary Value Problem. Symposium on Earth's Gravitational Field & Secular Variations in Position, pp. 475–488.

Burša M (1973a). Gaussian curvature of smoothed equipotential surfaces from satellite orbit dynamics, Studia geoph. et geod., (17), pp. 1–6.

Burša M. (1973b). The mean curvature of the external equipotential surface and the vertical gravity gradient as functions of Stokes's constants, Studia geoph. et geod., (17), pp. 74–80.

Burša M. (1973c). Geoidal curvature radii from satellite data for different degrees of smoothing, Studia geoph. et geod., (17), pp. 193–198.

Cevallos C., M. Dransfield, J. Hope and H. Carey (2012). Application of curvatures to airborne gravity gradients, ASEG Extended Abstracts, 2012, (1), pp. 1–6. DOI: 10.1071/ASEG2012ab270.

Cevallos C., P. Kovac and S.J. Lowe (2013). Application of curvatures and Poisson's relation to airborne gravity gradient data in oil exploration, ASEG Extended Abstracts, 2013, (1), pp. 1–4. DOI: 10.1071/ASEG2013ab112.

de Graaff-Hunter J. (1951). The Geodetic Uses of Gravity Measurements and their Appropriate Reduction. Proceedings of the Royal Society of London, Series A, Mathematical and Physical Sciences, 206 (1084), pp. 1–17.

Deakin R.E., (1998). Derivatives of the Earth's potentials, Geom Res Aust, 68, pp. 31–60.

Forsberg R. and C.C. Tscherning (2008). An overview manual for the GRAVSOFT Geodetic Gravity Field Modelling Programs. 2nd edn., National Space Institute (DTU–Space), Denmark, August, 2008.

Förste C., S.L. Bruinsma, F. Flechtner, J-C. Marty, J-M. Lemoine, C. Dahle, O. Abrikosov, H. Neumayer, R. Biancale, F. Barthelmes and G. Balmino (2012). A preliminary update of the Direct approach GOCE Processing and a new release of EIGEN-6C. Abstract No. G31B-0923, AGU Fall Meeting, San Francisco, December 3–7, 2012.

Gilardoni M., M. Reguzzoni and D. Sampietro (2016). GECO: a global gravity model by locally combining GOCE data and EGM2008, Studia geoph. et geod.,60 (2016), pp. 228–247. DOI: 10.1007/s11200-015-1114-14.

Hirvonen R.A. (1954). The Gravimetric Method for Determination of the Form of the Geoid, Tellus, VI (1954), 1, pp. 84–88.

Jekeli C. (2006). Geometric Reference Systems in Geodesy. Lecture Notes, Division of Geodesy and Geospatial Science, School of Earth Sciences, the Ohio State University.

Li X. (2015). Curvature of a geometric surface and curvature of gravity and magnetic anomalies, GEOPHYSICS, 80 (1), pp. 15–26. DOI: 10.1190/GEO2014-0108.1.

Liang W. (2018). SGG-UGM-1: the high resolution gravity field model based on the EGM2008 derived gravity anomalies and the SGG and SST data of GOCE satellite. GFZ Data Services. DOI: http://doi.org/10.5880/icgem.2018.001.

Livieratos E. and I. N. Tziavos (1991). Correlation of strain representations of the potential anomalies with the geoid. In Rapp, R.H. and F. Sansò (eds.), IAG Symposium106, Determination of the Geoid: Present and Future, Milan, Italy, June 11–13, 1990.

Mayer-Gürr T., D. Rieser, E. Höck, J. M. Brockmann, W. D. Schuh, I. Krasbutter, J. Kusche, A. Maier, S. Krauss, W. Hausleitner, O. Baur, A. Jäggi, U. Meyer, L. Prange, R. Pail, T. Fecher and T. Gruber (2012). The new combined satellite only model GOCO03S. Abstract presented at the International Symposium on Gravity, Geoid and Height Systems GGHS 2012, Venice, October 9–12, 2012.

Meyer T.H., D.R. Roman and D.B. Zilkoski (2004). What Does Height Really Mean? Part I: Introduction, Surveying and Land Information Science, 64(4), pp. 223–233.

Müller I., O. Holway and R. King (1963). Geodetic Experiment by Means of a Torsion Balance. Report No. 3, Institute of Geodesy, Photogrammetry and Cartography, the Ohio State University Research Foundation.

Raussen M. (2008). Elementary Differential Geometry: Curves and Surfaces. Department of Mathematical Sciences, Aalborg University, Denmark.

Reed G.B. (1973). Application of Kinematical Geodesy for Determining the Short Wave Length Components of the Gravity Field by Satellite Gradiometry. Report No. 201, Department of Geodetic Science, the Ohio State University.

Rummel, R. (1997). Spherical Spectral Properties of the Earth's Gravitational Potential and its First and Second Derivatives. In Sansò F. and R. Rummel (eds.), Geodetic Boundary Value Problems in View of the One Centimeter Geoid, Lecture Notes in Earth Sciences, 65, pp. 359–404.

Sansò F. and F. Sacerdote (2012). Marussi and the First Formulation of Physical Geodesy as a Fixed-Boundary-Value Problem. In Sneeuw N., P. Novák, M. Crespi and F. Sansò (eds.), VII Hotine-Marussi Symposium on Mathematical Geodesy, Rome, June 6–10, 2009, pp. 25–29.

Sharipov R.A. (2004). Course of Differential Geometry. Russian Federal Committee for Higher Education, Bashkir State University, Ufa, Russia.

Smith D.A. (1998). There is no such thing as "The EGM96 geoid": subtle points on the use of a global geopotential model, IGeS Bulletin, 8, pp. 17–28.

Smith D.A. (2010). Program geopot07. National Geodetic Survey. Available: http://ngs.noaa.gov. Accessed 12 February 2020.

Torge W. (2001). Geodesy, 3rd Edition. Walter de Gruyter Berlin.

Tscherning C.C., R.H. Rapp and C. Goad (1983). A comparison of methods for computing gravimetric quantities from high degree spherical harmonic expansions, Manuscr Geod, 8, pp. 249–272.

Tscherning C.C. (1976). On the chain-rule method for computing potential derivatives, Manuscr Geod, 1, pp. 125–141.

Tscherning C.C. (1981). Comparison of Some Methods for the Detailed Representation of the Earth's Gravity Field, Reviews of Geophysics and Space Physics, 19 (1), pp. 213–221.

Tscherning C.C. and K. Poder (1982). Some geodetic applications of Clenshaw summation, Boll Geofis Sci Aff, 4, pp. 351–364.

Tu L.W. (2017). Differential Geometry: Connections, Curvature, and Characteristic Classes. Springer International Publishing AG.346.

Vaníček P. and M. Santos (2019). What Height System Should be Used in Geomatics?, Int J Earth Environ Sci 4: 160. DOI: https://doi.org/10.15344/2456-351X/2019/160.

Völgyesi L. (2015). Renaissance of Torsion Balance Measurements in Hungary, Period. Polytech. Civil Eng., 59(4), pp. 459–464. DOI: 10.3311/PPci.7990.

Zhu L. (2007). Gradient Modeling with Gravity and DEM. Report No. 483, Department of Geodetic Science and Surveying, the Ohio State University.